Device

Article

Scalable, durable, and high-performance protonic ceramic fuel cell stacks manufactured by direct laser reactive additive manufacturing

Graphical abstract

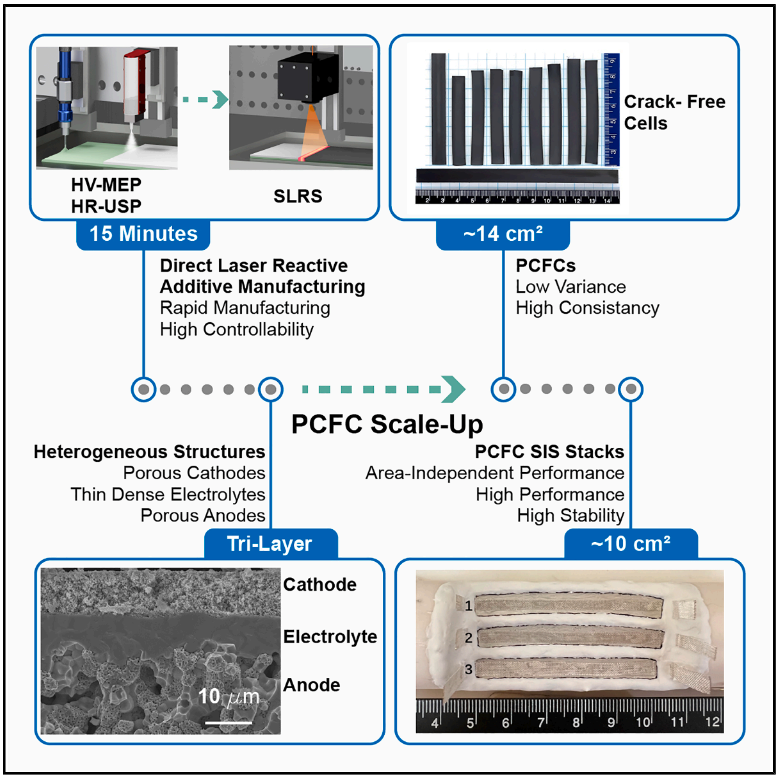

Highlights

- Laser-based additive manufacturing of high-performance protonic ceramic fuel cells
- Temperature gradients enable heterogeneous densification, ensuring high power output
- Stack production with area-independent performance, enabling large-scale operations
- Energy devices manufactured 150× faster than convention, aiding commercialization

Develop
Prototype with demonstrated applications in relevant environment

Authors

Hua Huang, Tianyi Zhou, Jacob Conrad, ..., Hai Xiao, Kyle S. Brinkman, Jianhua Tong

Correspondence

hhuang365@hotmail.com (H.H.), jianhut@clemson.edu (J.T.)

In brief

Huang et al. present protonic ceramic fuel cells (PCFCs) and stacks manufactured through the direct laser reactive additive manufacturing (DL-RAM) technique. These devices demonstrate constant power densities over a wide range of effective areas, long-term stability, and dimensional flexibility. The use of a high-power laser enables heterogeneous microstructures of dense electrolytes and porous electrodes to be produced in minutes as opposed to hours. These additively manufactured ceramic cells were integrated into large-area stacks, demonstrating high total power outputs.

Huang et al., 2025, Device *3*, 100840
September 19, 2025 © 2025 Elsevier Inc. All rights are reserved, including those for text and data mining, AI training, and similar technologies.
https://doi.org/10.1016/j.device.2025.100840

CellPress

Please cite this article in press as: Huang et al., Scalable, durable, and high-performance protonic ceramic fuel cell stacks manufactured by direct laser reactive additive manufacturing, Device (2025), https://doi.org/10.1016/j.device.2025.100840

Device

CellPress

Article

Scalable, durable, and high-performance protonic ceramic fuel cell stacks manufactured by direct laser reactive additive manufacturing

Hua Huang,[1,3,*] Tianyi Zhou,[1,3] Jacob Conrad,[1,3] Minda Zou,[1] Shenglong Mu,[1] Jianan Tang,[2] Yuqing Meng,[1] Zeyu Zhao,[1] Fei Peng,[1] Hai Xiao,[2] Kyle S. Brinkman,[1] and Jianhua Tong[1,4,*]

[1]Department of Materials Science and Engineering, Clemson University, Clemson, SC 29634, USA
[2]Department of Electrical and Computer Engineering, Clemson University, Clemson, SC 29634, USA
[3]These authors contributed equally
[4]Lead contact
*Correspondence: hhuang365@hotmail.com (H.H.), jianhut@clemson.edu (J.T.)

https://doi.org/10.1016/j.device.2025.100840

THE BIGGER PICTURE As global temperatures steadily increase, demand for clean energy production and storage climbs in response. While protonic ceramic fuel cells (PCFCs) stand out as highly efficient intermediate temperature electrochemical devices, there are serious limitations in commercialization due to current manufacturing difficulties. PCFCs manufactured through traditional means struggle with maintaining high performance with increasing area, showcasing a need for innovative ceramic production routes to enable large-scale implementation of PCFCs. Herein, we report a new ceramic additive manufacturing technique, direct laser reactive additive manufacturing (DL-RAM), for the production of large-area, stable, and power-dense PCFCs and stacks. Highly scalable, dimensionally flexible, and cost-effective PCFC production is enabled through commercially available oxide precursors, microextrusion-based 3D printing for anode production, ultrasonic spray printing for thin electrolyte layer application, and a unique laser-based densification method. This unique manufacturing route not only allows for cell production speed to be increased by a factor of 150× but also avoids the traditional pitfalls of furnace-sintered PCFCs, i.e., elemental segregation and over-densification. DL-RAM is applicable not only to PCFCs but also to a broad range of energy storage and conversion devices. The resulting single cells and stacks can be integrated into both portable and stationary clean energy systems, contributing to the development of a sustainable, green society. Beyond simple energy devices, DL-RAM stands as a foundational leap forward for layer-by-layer ceramic additive manufacturing, with broad implications for the future of additively manufacturing ceramics, both structural and functional.

SUMMARY

Protonic ceramic fuel cells offer higher efficiency, better stability, and lower costs than their counterpart energy devices, but their commercialization is far behind because of stack manufacturing and design challenges. This work solves layer thickness control, microstructure manipulation, and interfacial bonding challenges for multi-material heterogeneous ceramic additive manufacturing by a direct laser reactive additive manufacturing technique, which avoids multistep high-temperature furnace firing and enables on-demand manufacturing of protonic ceramic fuel cells down to minutes from around 80 h. This technique manufactures single cells with high power densities of around 1.03 W/cm^2 at 600°C, 2.6 times that of the conventionally processed ones. Furthermore, it realizes promising three- to six-cell segmented-in-series stacks with a peak power of 7 W and constant power output of 3.1 W for 260 h. A new on-demand ceramic additive manufacturing device and a practical energy conversion/storage device can be potentially derived from the current achievement.

INTRODUCTION

As global human power consumption rises alarmingly, the need for sustainable and clean energy conversion and storage technologies has never been more pressing. One promising solution is deploying protonic ceramic fuel cells (PCFCs).[1–6] This intermediate-temperature (350°C–650°C) cutting-edge energy device, schematically described in Figure 1A, offers many advantages,

All rights are reserved, including those for text and data mining, AI training, and similar technologies.

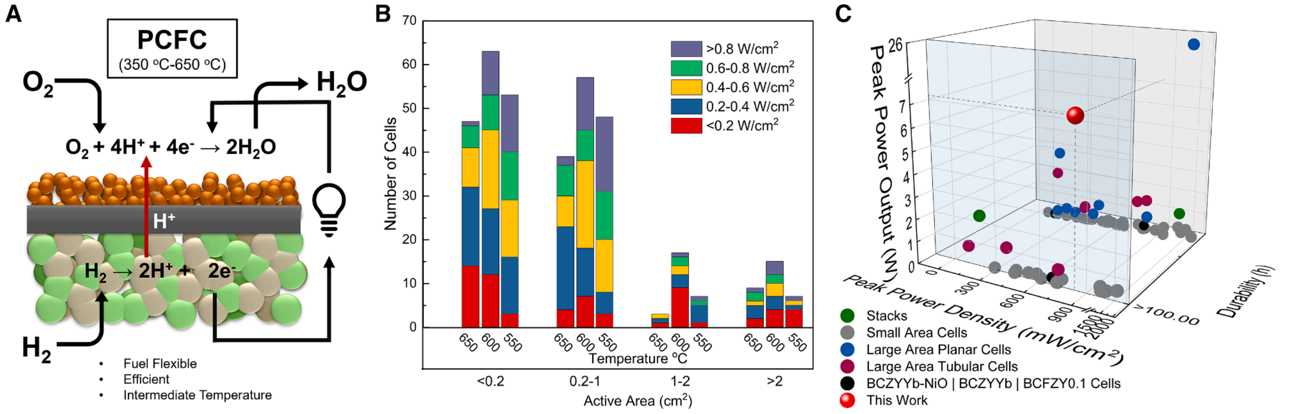

Figure 1. Working principle of PCFC and performance comparison of recently published PCFC works

(A) Working principle of the PCFC.

(B) The number of cells reported with peak power density (PPD) and their respective area over the past 10 years (2015–2025). Cell data used in this figure can be found in Table S1.

(C) A comparison of peak power output, peak power density, and durability of recently published PCFC small cells, stacks, and large-area tubes. Cells fabricated with the same materials as in this work are highlighted for direct comparison with those fabricated herein.

such as more agreeable operation temperatures, higher efficiencies, longer lifetimes, more fuel flexibility, longer thermal and chemical stabilities, better material compatibility, and lower cost of operation and materials,[7–9] over traditional low/high-temperature counterpart energy conversion storage devices, e.g., oxygen-ion-conducting solid oxide fuel cells (O-SOFCs, 700°C–1,000°C, Figure S1A) and polymer electrolyte membrane fuel cells (PEMFCs, around 80°C, Figure S1B). Although the scientific concept was conceived over 40 years ago, PCFCs started to make a significant performance breakthrough only in the past 10 years through the discovery of more efficient electrolyte/cathode materials, the engineering of more active microstructures and interfaces, and the development of moderate sintering techniques.[2,3,9–11] Some promising performances (e.g., peak power density) have demonstrated the ability of PCFCs to outperform O-SOFCs and PEMFCs at intermediate temperatures, attracting intensive attention from academics, governments, and industries.[12–15]

However, PCFCs' commercialization progress lags significantly behind O-SOFCs and PEMFCs, since the two counterpart devices have been demonstrated for either megawatt-scale power supply or fuel cell electric vehicles. At least three key factors of performance (high power density), stability (steady operation), and scalability (easy scaling-up) are the prerequisites for fuel cell devices to possess commercialization feasibility. Figure 1B and Tables S1 and S2 summarize the performance (peak power density) of PCFCs achieved in the past 10 years (2015–2025), which indicates that around 80% of the results were obtained from anode-supported small button cells with areas less than or equal to 1.0 cm^2. Although some peak power densities as high as 2.0 W/cm^2 have been reported at 600°C, the values fluctuated over 10–30 times, with a mean value of only 0.49 W/cm^2 at 600°C.[7,16,17] When comparing PCFCs fabricated from the same materials and identical procedures and cell architectures (Figure 1C, black dots, and Table S3), there is also a wide range of performance differences, suggesting PCFCs currently lack performance reproducibility. Figure 1C compares the performance, stability, and scalability of the most representative PCFCs. Regarding scalability, sporadic attempts have been made to increase the PCFC area using large planar cells/stacks and tubular cells/stacks. Beyond a singular large-area planar cell (16 cm^2) that demonstrated an impressive peak power density of 1.3 W/cm^2 at 600°C,[1] most other PCFC single cells (both planar and tubular) with an area larger than 1.0 cm^2 demonstrated mean power densities no higher than 0.45 W/cm^2 at 600°C. While seemingly simple stacks could increase effective area and total power output, there has been limited success. One representative three-cell planar PCFC stack from 5-cm^2 single cells was reported with a peak power density of only 0.23 W/cm^2 at 550°C,[18] encountering a dramatic drop compared to the single-cell performance. A two-cell tubular stack (8.2 cm^2) was reported but showed an output power density of only 0.28 W/cm^2 at 600°C, a nearly 50% reduction from the single-cell performance of 0.52 W/cm^2.[19] Another group demonstrated a sharp decrease from single tubular cell performance to stack performance, with a power density of 0.6 W/cm^2 at 700°C (0.43 cm^2) with a single cell down to 206 mW/cm^2 with a seven-cell stack (12.04 cm^2).[20] There are clear difficulties with maintaining the high performance of small-area single cells while increasing single-cell area and stack integration. While small-area single cells have shown impressive stability, limited reported stability data from multicell stacks indicate a distinct commercialization limitation. While PCFC development is promising, it is far from satisfying the simultaneous commercialization prerequisites of high performance, long stability, and easy scalability.

The technical challenges to satisfy these three PCFC commercialization prerequisites have become clearer in recent years. One such challenge is the extremely high required densification temperatures (e.g., 1,500°C–1,700°C) arising from the refractory nature of state-of-the-art perovskite-type protonic ceramic electrolytes.[9,15,21] These temperatures are much higher than those of O-SOFCs (e.g., 1,300°C–1,400°C), which causes many manufacturing challenges. The state-of-the-art PCFC manufacturing method of tape casting/furnace firing (Figure S2) involves organic-solvent-related ball milling, precursor calcination at moderate temperatures (900°C–1,400°C), tape casting, green half-cell lamination, half-cell sintering (i.e., co-firing) at high temperatures (1,500°C–1,700°C), cathode deposition, and cathode annealing at moderate temperatures (900°C–1,100°C).[22] The furnace processing steps, containing long-duration sintering under extremely high temperatures, lead to a high process energy, blunt electrolyte surfaces, highly resistive electrolyte/cathode interfaces, highly coarsened and densified anode microstructures, and the potential for inhomogeneous local properties due to uneven furnace temperature distribution[7,10,23] (Figure S3). These deleterious effects from high-temperature firing can all be ascribed to the poor reproducibility of small cells and the difficulty in attaining high-performing large-area cells. Another limitation arises from the large volume variations associated with the protonic ceramic electrolyte during hydration and dehydration. PCFC electrolytes require high proton conductivity and uptake for improved electrochemical performance, leading to a large expansion in lattice volume and stress across the cells. This inevitable stress is exacerbated in large-area cells and stacks, where there can be uneven fuel/oxidant distributions and temperature gradients over the cells. The established planar and tubular stack designs, where fuel distribution issues are well known, are particularly vulnerable to this issue, causing rapid failure, especially as single-cell area and cell count increase.[18,24–26] Therefore, to commercialize PCFCs, we must look beyond developing new materials and solve the intrinsic manufacturing challenges associated with high-temperature furnace densification while avoiding the shortcomings of popular planar and tubular stack designs.

To overcome the disadvantages of the popular planar and tubular stacks, namely problems with sealing, current collection, and hydration/thermal stresses, we can look to the unique stack architectures proposed for O-SOFCs, such as segmented in series (SIS), cone shape, flat tube, and many more exotic designs.[27–31] The SIS stack relies on multiple small-area planar single cells connected in series, typically over a porous ceramic membrane, through short interconnections to reduce ion and electron transport paths in a tubular or flat tubular orientation. As a hybrid of planar and tubular stacks, the SIS stack can afford high power densities associated with the short ionic and electronic transport paths and simple interconnects of planar stacks but can also simplify the sealing structures, similar to tubular stacks, all while improving structural stability due to the small single-cell size.[27,32,33] These benefits have been proven for O-SOFC stacks, including demonstrations of high performance, integration into kilowatt-scale stacks, and proof of thermal and redox stability.[34–38] Therefore, the SIS stack presents a more promising future for the scale-up of PCFCs by solving mechanical failure issues caused by large single cells. Typical O-SOFC SIS stacks are fabricated by screen printing the various functional layers and interconnectors onto a porous ceramic support, with multiple high-temperature firing steps.[39–41] The requirement of high-temperature furnace firing, problems with screen alignment/resolution, and possible stack failures due to the mis-manufacturing of a single cell lead to a tediously long manufacturing process. Therefore, though the SIS stack is a promising design, it is encountering significant manufacturing challenges, and the required high-temperature firing presents difficulties for PCFC commercialization.

The key obstacles to the commercialization of PCFCs converge into the manufacturing challenges caused by multiple high-temperature furnace firing steps required by state-of-the-art PCFC fabrication techniques. We must develop new manufacturing methods for PCFCs to avoid this fundamental issue. The recently erupted additive manufacturing (AM), or 3D printing, technologies have made significant progress. They are now used to manufacture practical products with desired geometries, high dimensional accuracies, various material properties, and various end functions.[42–47] Although AM technologies are widely successful in metal and polymer manufacturing, ceramic AM technologies are still very limited due to their unique material properties. Because of the mechanical limitations of ceramics, the commercially available ceramic AM devices all focus on printing complicated geometry in green bodies, followed by high-temperature furnace firing. To our knowledge, no commercial ceramic AM machines can consolidate a newly printed fresh layer on the previously sintered layers to manufacture the final geometry without post-firing. Ceramic AM technologies face four key challenges: (1) difficulty in bonding fresh layers and consolidated layers because ceramics usually don't melt into liquid, like metals and polymers; (2) difficulty in consolidating crack-free large-area layers because of the large thermal gradient coupled with ceramics' lack of plasticity; (3) difficulty in depositing layers with largely varied thickness; and (4) difficulty manipulating the microstructure layer by layer. Some AM technologies, however, such as inkjet printing, direct ink writing, binder jetting, and aerosol jet printing, have shown promise in fabricating O-SOFCs.[43,44,46–48] These ceramic AMs are usually limited to preparing green parts on a single support or thin-film component rather than the whole cell structure. Moreover, due to the refractory properties of state-of-the-art protonic ceramic electrolytes, PCFCs face much harsher manufacturing conditions than O-SOFCs. They require more exotic densification conditions, such as higher temperatures, longer sintering times, protective environments, sintering additives, and specific sintering techniques.[3,6,49] Because of these challenges, the AM of large-scale, multilayer, multimaterial PCFCs and stacks through conventional techniques is still unachievable.

In this work, by leveraging the AM and laser processing of protonic ceramics we have established in the last 10 years,[23,50–56] we develop and demonstrate the direct laser reactive AM (DL-RAM) method for high-performance SIS PCFC stacks. The unique advantages include (1) precisely size-controlled materials deposition and localized consolidation to form heterogeneous multilayer and multimaterial microstructures, (2) direct use of commercially available cost-effective raw materials, (3) a time-efficient and on-demand manufacturing process (e.g., a 10-cm^2 cell takes only 15 min), (4) a highly scalable and dimensionally flexible procedure, (5) avoidance of high-temperature furnace sintering, and (6) potential for direct manufacturing of stacks, including sealant and interconnect. The unique advantages afforded by the DL-RAM method allow for the creation of complex, layered SIS stacks with ease, without any of the restrictions associated with the traditional screen printing/furnace sintering

Please cite this article in press as: Huang et al., Scalable, durable, and high-performance protonic ceramic fuel cell stacks manufactured by direct laser reactive additive manufacturing, Device (2025), https://doi.org/10.1016/j.device.2025.100840

methodology, as well as improving the repeatability and reliability of stack production. By applying DL-RAM to the fabrication of PCFCs from model component materials of 60 wt % NiO + 40 wt % $BaCe_{0.7}Zr_{0.1}Y_{0.1}Yb_{0.1}O_{3-\delta}$ (BCZYYb) anode, BCZYYb + 1 wt % NiO electrolyte, and $BaCo_{0.4}Fe_{0.4}Zr_{0.1}Y_{0.1}O_{3-\delta}$ (BCFZY0.1) cathode, we manufactured PCFCs consisting of considerably porous nanostructured cermet anodes, dense electrolyte thin films with negligible grain boundary resistances and surface chemistry discrepancies, and highly nanoporous cathodes with well-bonded electrolyte/cathode interfaces, with ensuing power densities of ~1.03 W/cm^2 at 600°C under H_2/air, which is significantly higher than the documented single-cell performance manufactured using furnace-firing methods from the same materials. The DL-RAM method solved the stress issues associated with traditional ceramic AM by instant and localized sintering utilizing a partial liquid phase, achieving highly repeatable large-area crack-free half cells as large as 14 cm^2. We further developed the manufacturing ability of DL-RAM for SIS stack fabrication, demonstrating a seven-cell stack with an area close to 10 cm^2, output power of ~7 W, output open-circuit voltage (OCV) higher than 7 V, peak power density of 0.88 W/cm^2 at 650°C, and stable operation longer than 260 h. The DL-RAM method solves the challenges associated with SIS stack fabrication, ensuring a bright future for the commercialization of PCFCs, and enabling the manufacture of novel AM ceramic energy conversion/storage devices.

RESULTS AND DISCUSSION

Description of DL-RAM

Figure 2A schematically describes the DL-RAM technical concept for rapidly and precisely manufacturing heterogeneous ceramic devices (e.g., PCFCs) without post-processing steps beyond the DL-RAM station. The manufacturing method integrates some key techniques, such as high-volume microextrusion printing (HV-MEP), high-resolution ultrasonic spray printing (HR-USP), fast laser drying, selective laser reactive sintering (SLRS), and precise laser machining, into one highly compact AM device (Figure 2A, i). Video S1 shows typical processes for manufacturing a PCFC single cell using the DL-RAM method. HV-MEP is first used to print a homogeneous thick anode precursor layer from 40 wt % BCZYYb + 60 wt % NiO raw material paste onto a fused silica substrate. Then, HR-USP is used to print the BCZYYb + 1 wt % NiO electrolyte precursor slurry onto the green anode to form a thin electrolyte precursor layer. After drying by mild CO_2 laser or natural drying at room temperature, a high-energy CO_2 laser scan is used to sinter the anode/electrolyte bilayers to achieve rectangular half-cells through the movement of the *x-y* stage. The substrate de-binding, polymer burnout, and half-cell sintering happen in a single rapid laser scan with no adverse reactions. The key step for the successful manufacturing of large-area crack-free PCFC single cells is the high-energy CO_2 laser sintering of anode and electrolyte bilayers under a vertically distributed thermal gradient to achieve crack-free sintered half-cells with a thin, dense, and vertically grown large-grain electrolyte on a highly nanoporous anode. This methodology enables the fabrication of multiple cell architectures through a single DL-RAM manufacturing stage. The HV-MEP and HR-USP-combined layer deposition methods (Figure 2A, ii) allow accurate and rapid printing of green parts with well-controlled thicknesses, excellent flatness, and robust interlayer bonding. These manufacturing techniques integrate to make DL-RAM uniquely suitable for the AM of ceramic green parts. First, because of the relatively large nozzle size (e.g., 200 μm), HV-MEP can deposit thick layers, enabling a high production rate from pastes made of commercially available and cost-effective micrometer-sized ceramic powders without the need for sieving or other pre-processing. Second, the utilization of HV-MEP with low-viscosity paste coupled with fast laser drying not only allows the deposition of smooth and flat green ceramic planar layers as large as 100 cm^2 without hills or valleys between filaments (Figures S4) but also enables the printing of multilayered green parts with homogeneous thin walls and invisible bonding.[56] Third, HR-USP from a slurry of fine ceramic powders allows the deposition of thin green layers with well-controlled thicknesses down to 7 μm (Figure S5) through one deposition, introducing sintered layers with a thickness of less than 5 μm and excellent reproducibility (Figure S6). While highly suitable for green-part AM for PCFCs, DL-RAM's true strength lies in the SLRS methodology.

Instead of post-furnace firing after printing the complete green parts, SLRS (Figure 2A, iii) enables selective and rapid consolidation of the freshly deposited green layer on top of the previous layer through a vertical thermal gradient, which enables the formation of heterogeneous microstructures, quintessential for high PCFC performance. As schematically described in Figure 2B, SLRS integrates phase formation, solid-state sintering, and partial liquid-phase sintering into one manufacturing step. SLRS can achieve desired crystal structures for state-of-the-art PCFC electrolytes, cathodes, and anodes such as $BaZr_{0.8}Y_{0.2}O_{3-\delta}$, $BaCe_{0.6}Zr_{0.3}Y_{0.1}O_{3-\delta}$ (BCZY), BCZYYb, $BaCe_{0.4}Zr_{0.4}Y_{0.1}Yb_{0.1}O_{3-\delta}$, $BaCe_{0.7}Zr_{0.1}Y_{0.1}Sm_{0.1}O_{3-\delta}$, BCFZY0.1, and 40 wt % BCZYYb + 60 wt % NiO (Figure S7). Not only does SLRS produce phase-pure materials, but this technique also produces fully dense state-of-the-art protonic ceramic electrolytes such as BCZYYb, $BaCe_{0.4}Zr_{0.4}Y_{0.1}Yb_{0.1}O_{3-\delta}$, $BaCe_{0.7}Zr_{0.1}Y_{0.1}Sm_{0.1}O_{3-\delta}$, and $BaZr_{0.8}Y_{0.2}O_{3-\delta}$ (Figure S8). SLRS can easily manufacture highly dense electrolytes and produce porous structures from protonic ceramic materials for electrodes and electrode scaffolds (Figure S9) by lowering the laser power and optimizing the green layer composition. These gradient microstructures are difficult to obtain in a single piece through traditional AM. Furthermore, SLRS is capable of manufacturing multilayered components directly through the modification of green layer compositions and laser settings. As shown in Figure S10, increasing the distance (D) between the temperature probe and the laser focal surface results in a temperature drop, showcasing a vertical temperature gradient. This gradient enables SLRS to directly fabricate dual-layer half-cells consisting of an anode-supported electrolyte (Figure S11) and trilayer single cells comprising the anode, electrolyte, and cathode scaffold (Figure S12), all with excellent interlayer bonding and heterogeneous microstructures in a single laser scan—a critical advancement for both ceramic AM and PCFC development. While ceramics' brittle nature makes them difficult to manufacture additively, the use of reactive sintering introduces a well-documented partial liquid phase (BaY_2NiO_5)[13,57] in both the anode and the electrolyte layers (Figures 2B

Please cite this article in press as: Huang et al., Scalable, durable, and high-performance protonic ceramic fuel cell stacks manufactured by direct laser reactive additive manufacturing, Device (2025), https://doi.org/10.1016/j.device.2025.100840

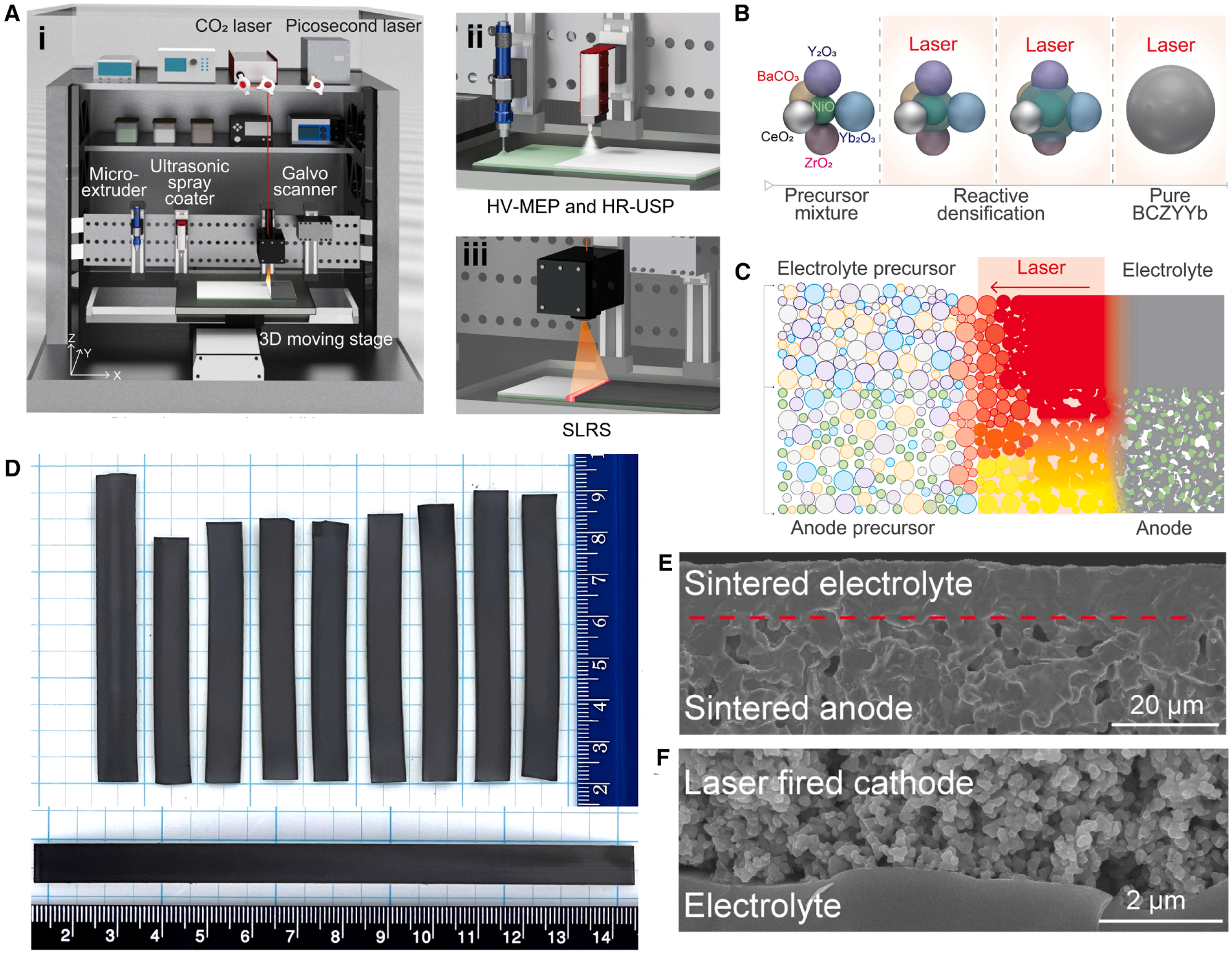

Figure 2. Schematic illustrations of DL-RAM technology and resulting example cells

(A) In (i), the entire DL-RAM system is showcased. In (ii), the schematic principle of anode layer printing by HV-MEP followed by electrolyte printing through HR-USP is demonstrated. In (iii), the SLRS schematic of the high-power CO_2 laser being scanned across the green half-cell produced in (ii) for densification is displayed.

(B) Densification and reaction of precursor powders exposed to SLRS, including partial liquid BaY_2NiO_5 at high temperatures.

(C) The schematic of the thermal gradient created by laser incidence on the electrolyte surface, which creates heterogeneous microstructures.

(D) Optical images of 10 DL-RAM-manufactured crack-free PCFC half-cells, with areas as large as 14 cm^2.

(E) SEM image displaying heterogeneous microstructures produced by a single laser scan, with a well-bonded dense electrolyte layer and the porous anode layer.

(F) Porous cathode well bonded to the dense electrolyte in one laser scan.

and 2C), which is hypothesized to act as a buffer region between densified and green bodies and layers, releasing the stress caused by a large horizontal thermal gradient during the laser scan. The localized heat generated by the laser causes binders to burn out just ahead of the sintering zone, resulting in partial detachment of the sintered layer from the substrate and forming a freestanding structure (Figure S13 and Video S1). This detachment facilitates stress relief during sintering, avoiding the typical issues associated with restrained sintering. Although the heating rate is high, the cooling rate remains relatively moderate (Figure S10B), which helps prevent crack formation. These combined effects enable the fabrication of large-area, multilayer, crack-free ceramic half-cells using laser processing. Furthermore, the galvo scanner produces a laser scanning line that is twice the width of the sample, effectively mitigating in-plane microstructural inconsistencies typically caused by the Gaussian intensity distribution of the laser spot. As shown in Figure S14, this approach ensures a consistent microstructure across both the edges and the center of the cells. Figure 2D summarizes 10 half-cells with a width of 10 mm and different lengths with representative desired microstructures of highly dense thin electrolyte layer well bonded to a porous anode support (Figure 2E), showing excellent manufacturing repeatability. The crack-free half-cells here have an area near 14 cm^2, which can be easily enlarged by increasing cell length or cell width with a higher laser power. While highly suitable for producing electrode scaffolds, the high-speed laser firing can also rapidly connect electrode nanoparticle necks without obvious grain growth to form a highly porous nanostructure for manufacturing cathode layers

Please cite this article in press as: Huang et al., Scalable, durable, and high-performance protonic ceramic fuel cell stacks manufactured by direct laser reactive additive manufacturing, Device (2025), https://doi.org/10.1016/j.device.2025.100840

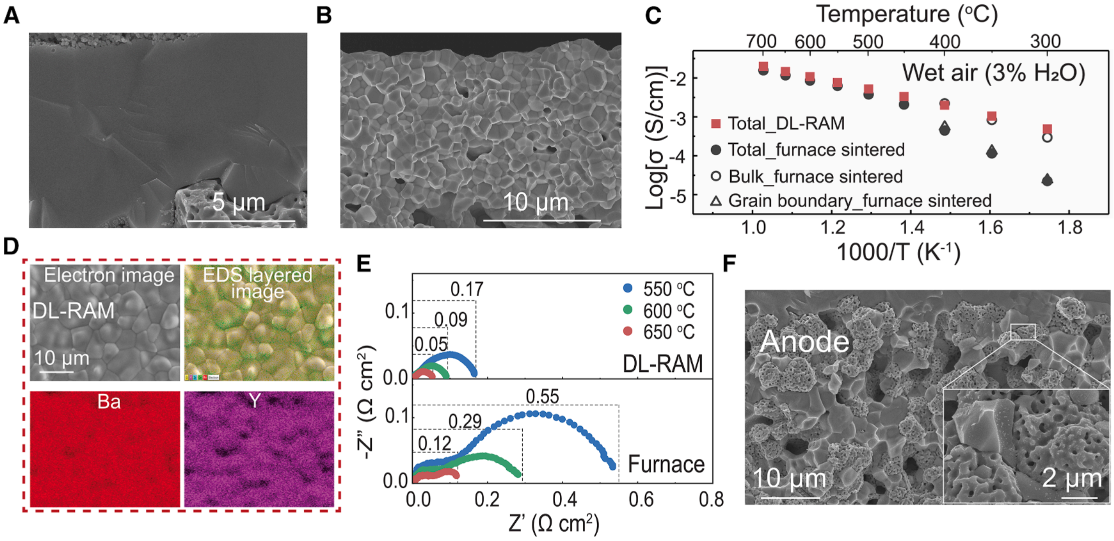

Figure 3. Microstructure and electrochemical characterization of DL-RAM half-cells and electrolytes

(A) Large grains and low grain boundary density in the DL-RAM electrolyte.

(B) Smaller grains and larger grain boundary densities were obtained by lowering laser power.

(C) Conductivity comparison between DL-RAM electrolyte and traditional furnace-sintered electrolyte.

(D) SEM-EDS images of SLRS electrolyte surface.

(E) EIS spectra of symmetric cells consisting of DL-RAM and traditional electrolytes with BCFZY0.1 cathode.

(F) Nano-sized pores and Ni nanoparticle precipitation are present on the DL-RAM anode after reduction.

directly. By adjusting the laser focus directly on the electrolyte surface, one can achieve higher temperatures at the electrolyte/cathode interface, creating the desired robustly bonded cathode and electrolyte (Figure 2F) without overdensification of the bulk electrode.

While the capabilities of DL-RAM are clear, the advantages become more evident through direct comparison with the state-of-the-art tape-casting/furnace firing method for manufacturing PCFCs. On production time alone, we can easily conclude that DL-RAM provides much faster on-demand manufacturing, nearly 150 times faster, with the largest reduction arising from the SLRS of PCFCs needing only ~15 min, depending on size, compared to over 18 h using the standard furnace firing methodology. Starting from pastes and slurry, the manufacturing process may be completed on one highly compact DL-RAM device without post-processing, making it suitable for autonomous manufacturing in a miniaturized space, due to the highly localized energy incidence. On the other hand, the conventional tape-casting/furnace firing method may need to handle the wet and high-temperature processes in different environments, adding significant difficulty for automation and miniaturization of the manufacturing process. Furthermore, DL-RAM allows the direct use of cost-effective raw materials, which can benefit the rapid consolidation process and significantly lower the cost of materials and processing. Finally, the rough electricity consumption for manufacturing 20 pieces of 5 × 5 cm^2 60 wt % NiO + 40 wt % BCZYYb|BCZYYb + 1 wt % NiO|BCFZY0.1 PCFCs in laboratories consumes electricity as high as ~270 kWh. In contrast, while producing the same amount of PCFCs, only 21% of the electricity will be consumed by DL-RAM manufacturing because of the shorter time, highly selective sintering, and fewer high-temperature processes (Figure S15 and Note S1).

Characterization of DL-RAM-manufactured PCFCs

The high grain boundary resistance for state-of-the-art perovskite-type electrolytes has been a key obstacle to the high performance of PCFCs for many years because it worsens with decreasing temperatures, limiting low-temperature performance. While the production of thin electrolyte films with large grains has been heavily studied and is well understood to improve PCFC performance, they can typically be produced only by high-temperature (>1,500°C) and long-duration (>10 h) furnace sintering. On the other hand, DL-RAM can increase grain size and decrease grain boundary thickness readily (Figures 3A and 3B) by increasing laser scanning energy density. The BCZYYb electrolyte grain size as large as 5–10 μm was obtained through SLRS. The large grains can significantly lower the grain boundary numbers perpendicular to the proton transport direction. Furthermore, it is commonly accepted that during laser AM, grains grow along the largest temperature gradient toward the hottest region,[58,59] as schematically described in Figure S16. This preferred grain growth direction can elongate the grains perpendicular to the electrolyte membrane, resulting in grain boundaries parallel to the proton transport direction, contributing to negligible electrical resistance for the parallel charge transport. The BCZYYb electrolyte film with this optimized bulk microstructure was characterized by electrochemical impedance spectroscopy (EIS) to understand proton transport properties at various temperatures under wet air. Figure S17 indicates that the EIS Nyquist arc ascribed to the conventional electrolyte's grain boundary transport process by the traditional furnace firing does not

Please cite this article in press as: Huang et al., Scalable, durable, and high-performance protonic ceramic fuel cell stacks manufactured by direct laser reactive additive manufacturing, Device (2025), https://doi.org/10.1016/j.device.2025.100840

emerge for the BCZYYb electrolyte film obtained by the SLRS. The total conductivity of the SLRS-manufactured BCZYYb electrolyte (Figure 3C) is almost the same as the bulk conductivity and much higher than the total and grain boundary conductivities of the traditional furnace-fired electrolyte containing many grain boundaries, reaching a high value of 14.6 mS/cm^2 at 600°C.

While the ionic conductivity of electrolytes is important for high performance, the electrolyte's surface properties also play a significant role. The surface chemistry discrepancy from bulk is well documented and was unavoidably observed for protonic ceramic electrolyte membranes (e.g., BCZYYb, Figure S3) manufactured by high-temperature and long-time furnace firing (1,500°C for 18 h; the necessary processing conditions for achieving desirable electrolyte bulk microstructure), which has been proven to be the reason for the poor interfacial kinetics between electrolyte and cathode.[10,23,60–62] Introducing a dense cathode nanolayer, acid etching of the electrolyte top surface, enhancement of the barium source, and digital laser texturing improved both ohmic resistance and cathode performance. However, they still face challenges of processing complexity and control difficulty. It is crucial, therefore, to look at changes in the sintering itself to mitigate this foundational issue. It has been demonstrated that ultra-fast sintering of ceramics at a temperature much higher than their conventional sintering temperatures could eliminate elemental migration and volatile element loss, including materials for O-SOFC electrolytes.[63,64] SLRS utilized by DL-RAM can satisfy this ultra-fast sintering by ramping the temperature to the recommended sintering temperature and beyond within tens of seconds. As seen in Figures 3D and S18, the scanning electron microscopy (SEM)-energy dispersive X-ray spectroscopy (EDS) analysis of the laser-sintered BCZYYb shows that neither the deficiency of Ba and Ce nor the enrichment of Y, Yb, or Zr was found on the smooth electrolyte surface. While the exact temperature reached during SLRS is currently being studied, the lack of elemental segregation and loss due to the ultra-fast sintering is evident, suggesting improved interfacial characteristics between the cathode and the DL-RAM electrolytes. To characterize this improvement, the state-of-the-art BCFZY0.1 cathode was deposited on both sides of a DL-RAM-manufactured BCZYYb + 1% NiO electrolyte thin film to form a symmetrical cell to investigate oxygen reduction reaction (ORR) area-specific resistances (ASRs) under oxidization atmosphere. Figure 3E, the comparison between symmetrical cells from DL-RAM-manufactured and furnace-firing-manufactured BCZYYb electrolytes, shows that the cathode ASRs (0.05, 0.09, and 0.17 Ω·cm^2 at 550°C, 600°C, and 650°C) for the symmetrical cell from DL-RAM-manufactured electrolyte improve significantly and are only about one-third of the values for the symmetrical cells from furnace-firing-manufactured electrolyte at all three measurement temperatures. The distribution of relaxation times (DRT) analysis of the corresponding EIS spectra revealed a reduced high-frequency (HF) contribution (Figure S19), suggesting an improved electrolyte/cathode interfacial exchange rate due to a superior electrolyte surface.[23] The EIS Nyquist plots of symmetrical cells with the same porous BCFZY0.1 layers on both defective surfaces of BCZYYb + 1 wt % NiO electrolytes further show the high cathode ASR (0.55 Ω·cm^2 at 550°C) and poor stability (degraded by about 120% after 15 h, Figure S20), while the cathode on the DL-RAM-manufactured electrolyte showed stable operation for more than 100 h in single cells (Figure 4D in next section). These results cement the ability of DL-RAM to produce superior electrolytes without any additional post-processing.

While the electrolyte difference between DL-RAM and furnace-fired samples is clear, we also investigated anode changes. During the long-duration co-firing in the high-temperature furnace required to achieve fully dense, large-grained protonic ceramic electrolytes, the anode is simultaneously densified and coarsened, resulting in poor anode microstructure. This can be seen in the common anode composition of 60 wt % NiO + 40 wt % BCZYYb after being co-fired at 1,500°C for 18 h through solid-state reactive sintering (Figure S21A), showcasing a fully dense microstructure. Even after reduction, there are limited pores resulting from the phase transition from NiO to Ni, and large BCZYYb (~10 μm) and Ni (~12 μm) grains are observed (Figure S21B), while the desired catalytically active Ni nanoparticles are not found, which usually is believed to be the reason for poor anode performance (Figure S21C). Not only are there significant microstructural issues, but reducing the dense composite structure often causes higher strain between the BCZYYb/Ni interfaces and significant volume change, which may form microcracks during cell performance testing, resulting in rapid degradation of the anode and single-cell performance (Figure S21D). The half-cells of the same anode and electrolyte manufactured by DL-RAM show much smaller grain sizes and higher porosity (Figure S22), resulting in highly nanoporous structures (Figure 3F) suitable for high performance after reduction. In addition, nickel nanoparticles that precipitated on the BCZYYb surface, which were extensively accepted to be responsible for fast hydrogen or hydrocarbon oxidation kinetics, were observed.

Evaluation of DL-RAM-manufactured PCFC single cells

To study the capabilities of DL-RAM for electrochemical device manufacturing and its impact on final electrochemical performance, three classes of PCFC single cells were prepared by introducing cathodes through different routes (Figure S23): S-cat (standard cathode), L-cat (laser-sintered cathode), and L-com-cat (laser-sintered composite cathode). Five DL-RAM-manufactured (with representative microstructures shown in Figure 4A) and one furnace-manufactured (with a representative microstructure shown in Figures S21 and S24) single cells were produced to evaluate the suitability of PCFC single cells for commercialization. Exact preparation techniques for each cell class can be found in the methods, and all PCFC single cells are summarized in Table S4.

As shown in Figure 4B, a small S-cat button cell (C-2) made from the DL-RAM-manufactured half-cell and standard cathode achieved peak power densities as high as 1,030, 692, 430, and 265 mW/cm^2 at 600°C, 550°C, 500°C, and 450°C, respectively (corresponding ASRs are shown in Figure S25). Compared with performance (peak power densities of 588, 443, 314, and 192 mW/cm^2 at 600°C, 550°C, 500°C, and 450°C) for the control cell (C-1) manufactured with the furnace-firing-based solid-state reactive sintering method (Figure S24A), the peak power densities of the DL-RAM cell increased tremendously, 2.55–2.67 times the control values. This is much higher than those for some recently

Please cite this article in press as: Huang et al., Scalable, durable, and high-performance protonic ceramic fuel cell stacks manufactured by direct laser reactive additive manufacturing, Device (2025), https://doi.org/10.1016/j.device.2025.100840

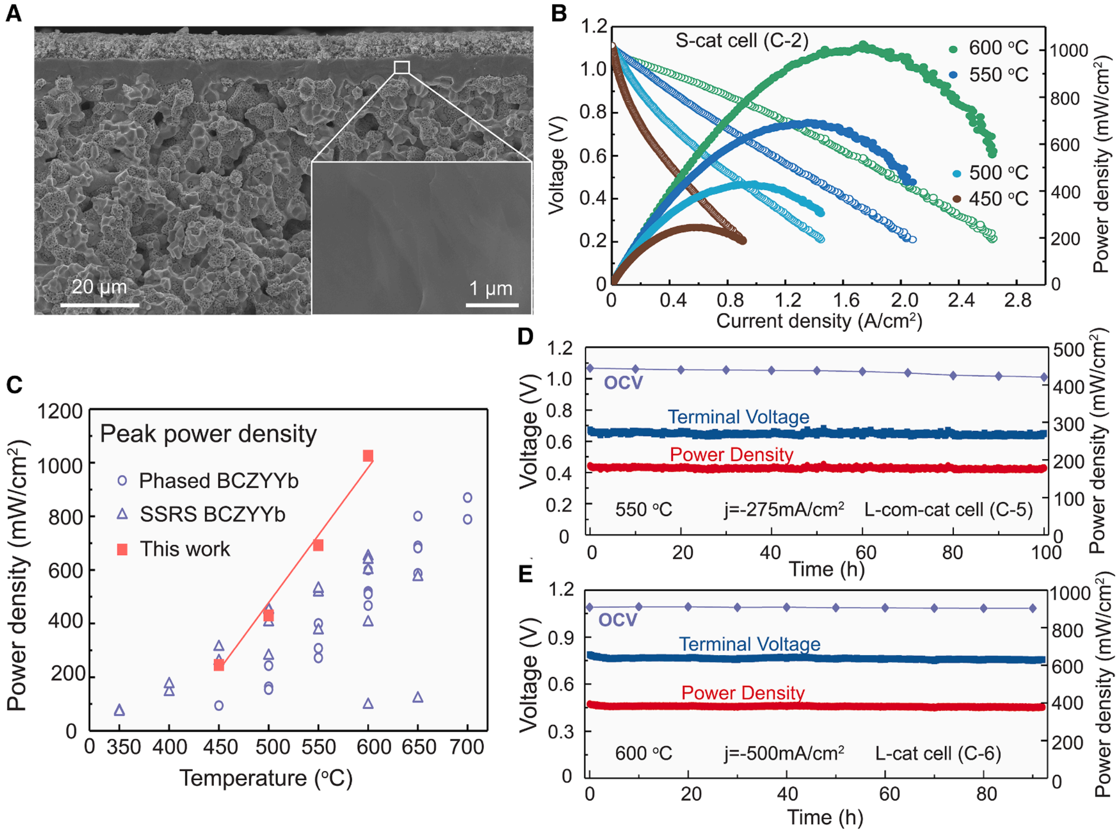

Figure 4. Microstructure and electrochemical characterizations of DL-RAM single cells

(A) SEM micrograph of a DL-RAM single cell cross section with near grain-boundary-free electrolyte and porous electrodes.

(B) Current density-power density (I-P) and current density-voltage (I-V) curves of the S-cat cell (C-2).

(C) PPD comparison between C-2 and recently published works with the same cell configuration.

(D) Stability testing data for C-5 for over 100 h drawing a constant current density of 275 mA/cm^2 at 550°C.

(E) More aggressive stability testing data of C-6 for over 90 h drawing a higher constant current density of 500 mA/cm^2 at 600°C.

reported PCFC single cells with similar components of 40 wt % BCZYYb + 60 wt % NiO anode, BCZYYb electrolyte, and BCFZY0.1 cathode fabricated using conventional furnace-co-firing methods (Figure 4C and Table S3).[3,19,65–70] To understand the superior performance of the DL-RAM-manufactured cells, we compared electrode ASRs with those of the control cell (Figure S24B). The DL-RAM-manufactured cell shows lower ASRs, corresponding to faster electrode kinetics, than the furnace-sintered control cell from the entire temperature range (e. g., the ASR decreased 63% at 600°C). The high-magnification SEM image of the cross section of the laser-sintered electrolyte does not have clear grain boundaries, ensuring high protonic conductivity (Figure 4A). In contrast, the furnace-sintered electrolyte's high-magnification SEM image shows clear grain boundaries and some residual closed pores (Figures S24C and S24D). Moreover, the direct anode microstructure comparison demonstrated that the laser-sintered anode has a higher porosity, smaller grain sizes, more nickel nanoparticles, and better interphase percolations than the furnace-sintered anode (Figures 3F and S24E). To quantify the improvement of anode microstructure, conventionally fired and laser-sintered half-cells were tested in a gas-adsorption analyzer to determine the porosity of each sample (Figure S26). Brunauer-Emmet-Teller (BET) analysis calculated a surface area per mass value of ~11.91 m^2/g for the conventional cell and ~28.01 m^2/g for the laser-sintered cell. This leads to an increase in gas diffusion in the anode layer and triple-phase boundary sites, which both improve cell performance.

Figures S27 and S28 provide the performance (I-V and I-P curves), ASRs, and SEM images of two other PCFC single cells of L-com-cat (C-3, 0.42 cm^2) and L-cat (C-4, 0.42 cm^2) with laser-processed cathodes. With normalization by electrolyte thickness, a similar performance with C-2 was achieved. Therefore, furnace processing can be completely avoided for the manufacturing of PCFCs, enabling the potential for autonomous, on-demand manufacturing out of the 3D printing stage. The DL-RAM-manufactured PCFC single cells were further evaluated for performance stability while drawing constant currents at certain temperatures (550°C–600°C). The stability test results (Figure 4D) of an L-com-cat cell (C-5, ~0.3 cm^2) at 550°C under an H_2/air gradient while drawing a current of 275 mA/cm^2 show no marked degradations of power density or terminal voltage for approximately 100 h. An L-cat cell with a larger area (~1.1 cm^2, C-6) was tested at a higher temperature of 600°C while drawing a higher current of 500 mA/cm^2. Although the output was as high

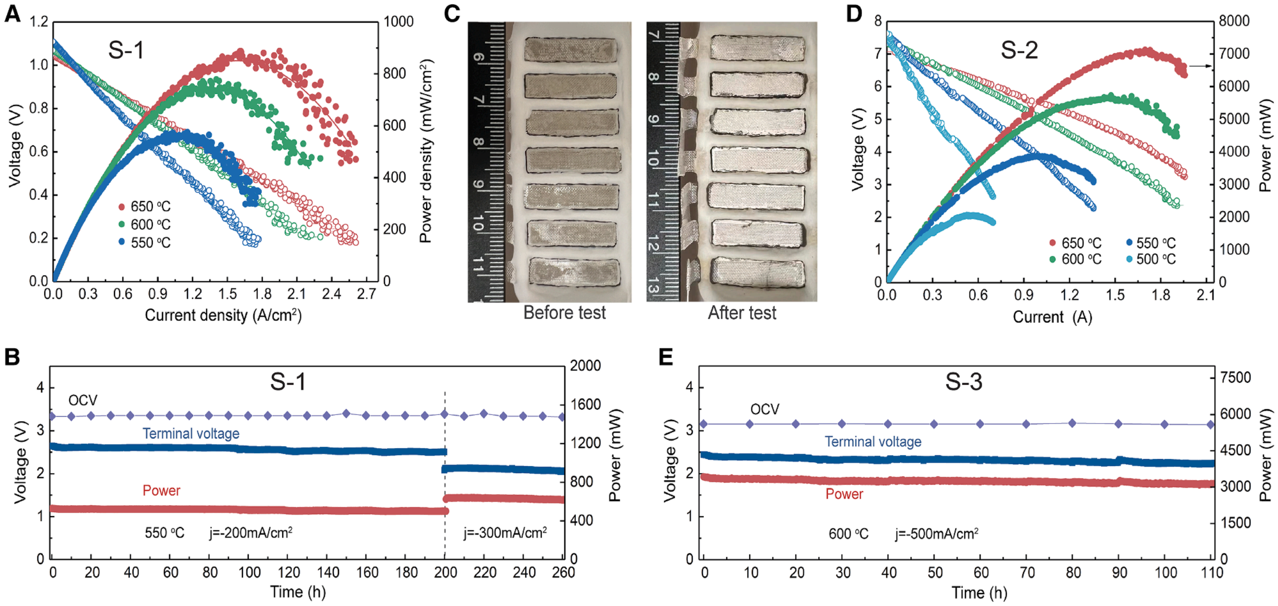

Figure 5. Electrochemical characterization and appearance of DL-RAM stacks

(A) I-P and I-V curves of S-1.

(B) Stability testing data for S-1 for 200 h drawing constant current density of 200 mA/cm^2 at 550°C followed by an increase of current density to 300 mA/cm^2 for an additional 60 h.

(C) Optical images of S-2 before and after performance testing show no obvious signs of stack failure or degradation.

(D) I-P and I-V curves of S-2.

(E) Stability testing of large-area S-3 drawing constant current density of 500 mA/cm^2 for over 100 h at 600°C.

as ~0.4 W (about seven times C-5), the power density and terminal voltage did not degrade for approximately 92 h (Figure 4E). The unchanged OCV versus time for both cells proved that no leakage-related cracks occurred across the cells or through the sealing regions during long-term operation. Figures S9, S12, and S29 provide a detailed microstructure comparison of the cathode, electrolyte, anode, and electrode/electrolyte interfaces between the fresh and the long-term-tested cells. Almost all identical microstructures were observed for the L-com-cat and the L-cat cells before and after the long-term test, which can explain the stable performance of these two cells while outputting the desired power.

Evaluation of DL-RAM-manufactured SIS PCFC stacks

Following demonstrations of stability and high performance, we investigated the validity of DL-RAM for large-area stack production. Due to the discussed problems with tubular and planar stacks, we implemented an SIS stack architecture (Figure S30). These problems are all addressed using the DL-RAM methodology. As discussed, DL-RAM uniquely avoids the long-duration high-temperature furnace firing, HR-USP provides resolution for electrolytes down to <6 μm, and the HV-MEP allows for each cell in the stack to be additively manufactured individually, preserving the stack structure if one cell were to fail. Three SIS stacks (Table S5) with different cell configurations were fabricated to analyze the feasibility of DL-RAM.

The individual S-cat cells of around 1 cm^2 were constructed in a three-cell stack (S-1, ~3 cm^2) and tested to prove the feasibility of DL-RAM for SIS production (Figure S31A). The performance testing results (Figure 5A) of S-1 show that the peak power densities of 888, 779, and 576 mW/cm^2 were achieved at 650°C, 600°C, and 550°C, respectively, which is consistent with the performances measured for the single cells. The stability testing results (Figure 5B) show that the stack could output a constant power of ~0.5 W and a steady terminal voltage of ~2.5 V for 200 h while drawing a constant current of 200 mA/cm^2 at 550°C. After drawing an increased current of 300 mA/cm^2, within the additional operation of 60 h, the constant power output of ~0.6 W and a steady terminal voltage of ~2.1 V were successfully achieved. The steady OCV of ~3.4 V and the almost undegraded microstructures (Figures S31B–S31E) of the cell components for all the cells constructed into the stack explain the excellent stability.

To further study the scalability and area independence of the performance, a seven-cell stack (S-2) with a total area of ~9.3 cm^2 was constructed from seven S-cat cells with an average single-cell area of around 1.3 cm^2 (Figure 5C). The stack performance (I-V and I-P curves) at 650°C–500°C under H_2/air gradient (Figure 5D) indicates peak power outputs as high as 7.157, 5.728, 3.887, and 2.071 W at 650°C, 600°C, 550°C, and 500°C, respectively. The peak power densities normalized by the smallest cell area are 810, 648, 440, and 234 mW/cm^2, which are also very consistent with power densities obtained from stack 1 and other individual cells under the same testing conditions due to the high cell structure reproducibility provided by the DL-RAM method (Figure S32). A three-cell stack (S-3, ~8.7 cm^2) was

Please cite this article in press as: Huang et al., Scalable, durable, and high-performance protonic ceramic fuel cell stacks manufactured by direct laser reactive additive manufacturing, Device (2025), https://doi.org/10.1016/j.device.2025.100840

constructed from individual S-cat cells with a larger area of ~2.9 cm^2 (Figure S33A) to further test scalability and area independence of performance. Figure S33B provides the performance (I-V and I-P curves) for S-3. Powers of 6.931, 5.91, 4.196, and 2.365 W and OCVs of 2.99, 3.11, 3.21, and 3.29 V were obtained at 650°C, 600°C, 550°C, and 500°C, respectively. The power densities normalized by the smallest cell area of 2.8 cm^2 are 825, 705, 500, and 281 mW/cm^2, again consistent with the performances of the other cells and stacks. Stack stability was tested for S-3 to study the effect of increased individual cell area, stack area, and power output on stack performance. Figure 5E indicates that a stable power of around 3.1 W could be output for around 110 h while drawing a constant current of 500 mA/cm^2 and keeping a steady terminal voltage of ~2.3 V at 600°C. The stable OCVs and undegraded microstructures (Figures S33C–S33F) for cell components of the stack cells explain the excellent stack stability. Figure S34 further compared the PCFC cell/stack performance achieved by DL-RAM with the reported ones summarized in Table S1. It is clear that the DL-RAM achieved area-independent electrolyte conductivity and electrode ASR, resulting in area-independent power density while considering the same electrolyte thickness.

Conclusion

In conclusion, the DL-RAM technique enables the fabrication of additively manufactured high-performance PCFCs without traditional high-temperature and long-duration furnace firing steps, significantly reducing the overall fabrication time and improving the microstructures. Rapid and precise layer deposition is achieved through the HV-MEP and HR-USP processes. The partial liquid phase sintering and temperature gradient present during SLRS enable crack-free, large-area (e.g., 14 cm^2) sintering of PCFC half-cells and full cells with desired heterogeneous layer microstructures and improved electrolyte/electrode interfaces. The fabricated single cells achieved power densities as high as 1,030 mW/cm^2 at 600°C, a benchmark for cells with the same materials. SIS stacks with areas as large as 9.3 cm^2 demonstrated total power outputs of up to 7 W and constant power outputs of up to 260 h. Furthermore, the PCFCs and stacks exhibited highly area-independent performance and durability, highlighting the scalability and commercial potential of the DL-RAM technique. The underlying principles of DL-RAM also offer broad applicability in the manufacturing of complex ceramic and ceramic/metal composite structures, making it a promising fabrication technique for energy conversion and storage devices such as fuel cells, electrolyzers, and solid-state batteries, as well as a leap forward for layer-by-layer ceramic AM.

METHODS

Materials and paste/suspension preparation

Anode precursor paste

BCZYYb with NiO (40:60 wt %) was selected as the anode electrode. According to the composition of BCZYYb, stoichiometric amounts of the precursor solids of $BaCO_3$ (Thermo Fischer), CeO_2 (Thermo Fischer), ZrO_2 (Alfa Aesar), Y_2O_3 (Thermo Fischer), Yb_2O_3 (Alfa Aesar), and 60 wt % of NiO (Alfa Aesar) (based on the BCZYYb weight) were mixed by roller ball milling for 48 h with isopropanol solvent and 3-mm YSZ grinding medium in a Nalgene bottle. They were then dried to remove the isopropanol at 90°C for 24 h. After that, 15 wt % de-ionized (DI) water solvent and 1.5 wt % dispersant (Darvan 821A, Vanderbilt Minerals) were added to the dry precursor powders, and the slurry was ball milled for 24 h with 3-mm YSZ grinding medium. Binder (HPMC, 0.25%, Alfa Aesar) was added to the paste and mixed using a planetary centrifugal vacuum mixer (MTI, MSK-PCV-300-LD) for 30 min at 1,000 rpm and −90 kPa to obtain a homogeneous and bubble-free anode precursor powder paste.

Electrolyte precursor suspension

The BCZYYb suspension was prepared using stoichiometric amounts of the precursor solids $BaCO_3$ (Thermo Fischer), CeO_2 (Thermo Fischer), ZrO_2 (Alfa Aesar), Y_2O_3 (Thermo Fischer), and Yb_2O_3 (Alfa Aesar). NiO (1 wt %, Alfa Aesar) sintering additive was mixed with those precursors by roller ball milling for 48 h with isopropanol solvent and 3-mm YSZ grinding medium in a Nalgene bottle. It was then dried at 90°C for 24 h to remove the isopropanol. The dried powders were mixed with 45 wt % ethanol, 5 wt % binder (5 wt % V-006 [Heraeus] dissolved in terpinol), and 5 wt % dispersant (triethanolamine, Thermo Fischer) for 48 h of ball milling before spraying.

Cathode scaffold precursor suspension for L-com-cat cell

The BCZY63 suspension was prepared using stoichiometric amounts of the precursor solids $BaCO_3$ (Thermo Fischer), CeO_2 (Thermo Fischer), ZrO_2 (Alfa Aesar), and Y_2O_3 (Thermo Fischer). Fe_2O_3 (1 wt %, Alfa Aesar) sintering additive and 45 wt % starch (Thermo Scientific) were added, and the mixture was roller ball milled for 48 h with isopropanol solvent and 3-mm YSZ grinding medium in a Nalgene bottle. It was then dried at 90°C for 24 h to remove the isopropanol. The dried powders were ball milled with 65% ethanol and 3 wt % dispersant (triethanolamine, Thermo Scientific) for 24 h, then 1.5% Butvar (B-98), 1.5% Di-n-butyl phthalate, and 1.5% polyethylene glycol 600 were added to the suspension for another 24 h of ball milling.

Cathode infiltration solution for L-com-cat cell

The BCFZY0.1 cathode solution was prepared using stoichiometric amounts of $Ba(NO_3)_2$ (Alfa Aesar), $Co(NO_3)_2{\cdot}H_2O$ (Alfa Aesar), $Fe(NO_3)_3{\cdot}9H_2O$ (Alfa Aesar), 35 wt % $ZrO(NO_3)_2$ in dilute nitric acid (Sigma Aldrich), and $Y(NO_3)_3{\cdot}6H_2O$ (Alfa Aesar) (0.015 mol total metal ion concentration) dissolved in 90 mL DI water. Citric acid (0.75 mol) was added as a complexing agent to facilitate the homogeneous distribution of the component metal ions.

Cathode precursor paste for S-cat cell

BCFZY0.1 precursor cathode powders were synthesized by the sol-gel method. The calculated stoichiometric amounts of $Ba(NO_3)_2$ (Alfa Aesar), $Co(NO_3)_2{\cdot}H_2O$ (Alfa Aesar), $Fe(NO_3)_3{\cdot}9H_2O$ (Alfa Aesar), 35 wt % $ZrO(NO_3)_2$ in dilute nitric acid (Sigma Aldrich), and $Y(NO_3)_3{\cdot}6H_2O$ (Alfa Aesar) were dissolved in EDTA (Alfa Aesar)-NH_3H_2O (Alfa Aesar) solution under continuous heating and stirring. Then citric acid was introduced, with the molar ratio of EDTA acid:citric acid:total metal ions controlled to be around 1.5:1.5:1. Subsequently, NH_3H_2O or HNO_3 was used to adjust the pH value to around 9. After the solution became clear, the water was evaporated. Then a dark purple gel was obtained and put into an oven at 150°C for 24 h to obtain

Please cite this article in press as: Huang et al., Scalable, durable, and high-performance protonic ceramic fuel cell stacks manufactured by direct laser reactive additive manufacturing, Device (2025), https://doi.org/10.1016/j.device.2025.100840

the primary powders. The powders were roller ball milled with butanol for 48 h with 3-mm YSZ medium in a Nalgene bottle, then dried at 90°C for 24 h, roller ball milled with isopropanol for 24 h again, and then dried at 90°C for 24 h. After that, the powders were calcined at 600°C for 5 h to obtain BCFZY powder. The powders were mixed with 15 wt % dispersant (20 wt % solsperse 28000 [Lubrizol] dissolved in terpinol) and 5 wt % binder (5 wt % V-006 [Heraeus] dissolved in terpinol) to fabricate cathode paste.

Cathode spray coating suspension for L-cat cell

The sol-gel method-synthesized BCFZY0.1 precursor powder was calcined in a furnace at 850°C for 5 h. Then the powders were mixed with 56% ethanol and 12.5 wt % dispersant (20 wt % solsperse 28000 [Lubrizol] dissolved in 3 terpinol) and 12.5 wt % binder (5 wt % V-006 [Heraeus] dissolved in terpinol) and underwent 48 h roller ball milling before spraying.

Half-cell fabrication

The anode precursor paste was extruded onto a fused silica substrate with a thickness of 0.3 mm utilizing HV-MEP (preeflow eco-PEN 300, ViscoTec). The electrolyte precursor was then applied to the surface of the printed anode using HR-USP. Then both layers were dried at room temperature in air. The CO_2 laser (Iradion 1625, wavelength ~10.6 μm) was directed through a galvo scanner (intelliSCAN III 14, SCANLAB) and focused onto the anode/electrolyte bilayer sample for laser sintering. Laser operation was at 0.1 mm/s scan speed, 45-cm gap (the distance between the galvo scanner and the sample), 15-mm scanning width, and 200 W laser power.

Single-cell fabrication

S-cat cell

The cathode precursor paste was brush printed by hand on the laser-sintered BCZYYb half-cell surface. Cathode layer thickness was controlled by brushed cathode slurry weight (0.6 $\mu g/cm^2$) and then sintered in a furnace at 900°C for 5 h.

L-com-cat cell

A BCZY63 cathode scaffold precursor suspension was deposited on the sintered BCZYYb half-cell surface by HR-USP. The three-layer sample was sintered by laser again (laser parameters were the same as for half-cell sintering). Then the BCFZY0.1 precursor solution was infiltrated into the pores of the L-cat bone structure under vacuum using a microliter syringe to control the loading amount (15 $\mu L/cm^2$). Next, the infiltrated cells were fired at 400°C for 1 h, and the above vacuum infiltration process was repeated five more times. Finally, the cells were sintered at 900°C for 1 h to obtain the desired nanocrystalline phase of BCFZY0.1.

L-cat cell

A BCFZY0.1 cathode spray coating suspension was deposited on the sintered BCZYYb half-cell surface by the ultrasonic spray coating head, and the samples were sintered by laser again. The laser bonding parameters were 0.1 mm/s scan speed, 45-cm gap, 15-mm width, and 120 W power.

Control cell

The anode precursor powder was mixed with starch (30 wt %) by dry ball milling for 48 h. This powder was pressed into green pellets under 350 MPa for 120 s in a circular carbon-aided steel die set. The electrolyte precursor suspension was deposited on the pressed anode by HR-USP. The pellets were sintered in a furnace at 1,500°C for 18 h. The cathode precursor paste was brush painted on the sintered BCZYYb half-cell surface and then bonded in a furnace at 900°C for 5 h.

Electrolyte sample fabrication for conductivity measurement

Furnace-sintered BCZYYb electrolyte

The BCZYYb + 1 wt % NiO electrolyte precursor powders were pressed into 12-mm-diameter green pellets under 350 MPa for 120 s in a circular carbon-aided steel die set. Then the pellets were sintered in a furnace at 1,450°C for 18 h.

Laser-sintered BCZYYb electrolyte

The BCZYYb + 1 wt % NiO electrolyte precursors were mixed with 15 wt % DI water and the 1.5 wt % dispersant (Darven 821A, Vanderbilt Minerals) and ball milled for 24 h with 3-mm YSZ grinding medium. Binder (HPMC, 0.25%, Alfa Aesar) was added to the paste and mixed using the planetary centrifugal vacuum mixer (MSK-PCV-300-LD, MTI) for 30 min to obtain a homogeneous and bubble-free electrolyte precursor powder paste. Next, the paste was extruded onto a substrate by a microextruder following the same procedure as the anode printing. After drying in air, the CO_2 laser was applied through a galvo scanner. The laser operation parameters used the same conditions as half-cell fabrication.

Symmetrical cell fabrication

The BCFZY0.1 cathode precursor paste was screen printed on both sides of the furnace-sintered BCZYYb electrolyte and laser-sintered BCZYYb electrolytes and was bonded in a furnace at 900°C for 5 h to obtain the symmetrical cells.

Temperature gradient testing

A platinum-rhodium temperature probe (B-type exposed thermocouple, Evolution Sensors and Controls) was placed on a fused silica substrate. An anode slurry composed of BCZYYb and NiO (40:60 wt %) was tape cast at varying thicknesses above the temperature probe (0.3, 0.8, 1.3, and 5.3 mm) to embed the temperature probe. The laser was focused on the top surface of the cast layer and scanned at a speed of 0.1 mm/s, starting from a distance of 2 cm away and moving toward the probe. Temperature data were recorded at 1-s intervals over a 25-s duration for both the heating (approaching) and the cooling (receding) stages.

Performance testing

Symmetrical cell testing

Silver paste and silver wire were used as a current collector using the four-point probe measurement technique, and a silver lead wire was attached to the BCFZY0.1 surface. The symmetrical cells were put in a testing furnace and tested in a wet air (3% H_2O) atmosphere (through a room temperature water bubbler, 50 mL min^{-1}). The ASR of the symmetrical cells was measured by potentiostat EIS spectra of a Reference 600 Plus (Gamry Instruments) with a signal amplitude of 10 mV in the frequency range of 0.05 Hz–5 MHz.

Conductivity measurement

Silver paste was attached to both sides of the electrolyte as a current collector, and silver wire was used as the lead wire. Then electrolyte samples were put in a testing furnace and tested in a wet air (3% H_2O) atmosphere at 300°C–700°C. The ASR of laser- and furnace-sintered BCZYYb electrolyte was measured by potentiostat EIS spectra of a Reference 600 Plus (Gamry Instruments) with a signal amplitude of 10 mV in the frequency range of 0.05 Hz–5 MHz.

Single-cell testing

All cells used silver paste as a current collector and silver wire as the lead wire using the four-point probe measurement technique. Ceramabond (552-VFG-1239, AREMCO) was used to mount and seal the single cell on an alumina testing rig. PCFC single cells were first heated to 100°C at a rate of 2°C/min and held for 1 h and then heated to 300°C at the same ramp rate and held for another 1 h to cure the sealant. After that, cells were increased to 550°C at a ramp rate of 1.5°C/min. Both the anode and the cathode were exposed to stagnant air during the heating process. H_2 at 5% (balance with Ar) and at 20 mL/min was fed into the anode through a room temperature water bubbler for the first 6 h and then switched to 20% H_2 (balance with Ar) for another 4 h. After that, the pure hydrogen was fed to the anode for 1 h. Air was swept over the cathode at 200 mL/min. After reduction, the temperature was increased to the highest required temperature at a rate of 2°C/min, at which point the required electrochemical data were collected. The performance of single cells was assessed by a Reference 3000 (Gamry Instruments) with cyclic voltammetry, potentiostat EIS (0.05 Hz–1 MHz), and OCVs.

Stack testing

Silver paste and silver mesh were used as a current collector using the four-point probe measurement technique. The single cells in each segment of stack were wired together, anode to cathode, in series using silver mesh, with the gaps between them sealed with Ceramabond (552-VFG-1239, AREMCO), and silver wire used as a lead wire. All cells in series were sealed on an alumina testing set. The temperature ramp-up process was the same as for single-cell testing. H_2 at 5% (balance with Ar) and at 100 mL/min was fed into the anode through a room temperature water bubbler for the first 6 h and then switched to 20% H_2 (balance with Ar) for another 4 h. After that, pure hydrogen was fed to the anode for 1 h. Cathodes were exposed to stagnant air. After reduction, the temperature was increased to the highest required temperature at a rate of 2°C/min, at which point the required electrochemical data were collected. The performance of single-cell stacks was assessed by a Reference 3000 (Gamry Instruments) with cyclic voltammetry, potentiostat EIS (0.05 Hz–1 MHz), and OCVs.

Microstructural and crystal structure characterization

The microstructures were characterized using a scanning electron microscope (Hitachi 8230, Hitachi Ltd). Elemental composition was detected by the EDS component on the Hitachi 8230. The crystal structure of each protonic ceramic component film prepared by SLRS was characterized by X-ray diffraction (MiniFlex, Rigaku). Gas adsorption and desorption isotherm curves and BET analysis were generated by the Autosorb iQ nitrogen gas adsorption analyzer (Anton Paar).

RESOURCE AVAILABILITY

Lead contact

Requests for further information, resources, and data should be directed to and will be fulfilled by the lead contact, Jianhua Tong (jianhut@clemson.edu).

Materials availability

All materials and manufacturing methods are reported herein.

Data and code availability

This article does not have any code to report. Any additional information required to reanalyze the data reported in this report is available from the lead contact upon request.

ACKNOWLEDGMENTS

This material was based upon work supported by the US Department of Energy's Office of Energy Efficiency and Renewable Energy (EERE) under the Fuel Cell Technologies Office award no. DE−EE0008428. This work was also partially supported by the US Department of Energy, Office of Science, Office of Basic Energy Sciences under award no. DE-SC0023407 and supported by the US Department of Energy's Office of Fossil Energy and Carbon Management (FECM) under award no. DE-FE0031871.

AUTHOR CONTRIBUTIONS

Conceptualization, H.H. and J. Tong; methodology, H.H., T.Z., J.C., and J. Tong; investigation, H.H., T.Z., J.C., M.Z., S.M., J. Tang, Y.M., and Z.Z.; writing – original draft, H.H., T.Z., J.C., and J. Tong; writing – review & editing, H.H., T.Z., J.C., and J. Tong; funding acquisition, F.P., H.X., K.S.B., and J. Tong; supervision, F.P., H.X., K.S.B., and J. Tong.

DECLARATION OF INTERESTS

The authors declare no competing financial interests.

DECLARATION OF GENERATIVE AI AND AI-ASSISTED TECHNOLOGIES IN THE WRITING PROCESS

The authors declare no use of generative AI tools in the production of this article.

SUPPLEMENTAL INFORMATION

Supplemental information can be found online at https://doi.org/10.1016/j.device.2025.100840.

Received: April 6, 2025
Revised: May 16, 2025
Accepted: June 2, 2025

REFERENCES

1. An, H., Lee, H.W., Kim, B.K., Son, J.W., Yoon, K.J., Kim, H., Shin, D., Ji, H.I., and Lee, J.H. (2018). A 5 x 5 cm2 protonic ceramic fuel cell with a power density of 1.3 W cm2 at 600 °C. Nat. Energy *3*, 870–875. https://doi.org/10.1038/s41560-018-0230-0.
2. Choi, S., Kucharczyk, C.J., Liang, Y., Zhang, X., Takeuchi, I., Ji, H.I., and Haile, S.M. (2018). Exceptional power density and stability at intermediate temperatures in protonic ceramic fuel cells. Nat. Energy *3*, 202–210. https://doi.org/10.1038/s41560-017-0085-9.
3. Duan, C., Tong, J., Shang, M., Nikodemski, S., Sanders, M., Ricote, S., Almansoori, A., and O'Hayre, R. (2015). Readily processed protonic ceramic

Please cite this article in press as: Huang et al., Scalable, durable, and high-performance protonic ceramic fuel cell stacks manufactured by direct laser reactive additive manufacturing, Device (2025), https://doi.org/10.1016/j.device.2025.100840

fuel cells with high performance at low temperatures. Science *349*, 1321–1326. https://doi.org/10.1126/science.aab3987.

4. Liu, F., Deng, H., Diercks, D., Kumar, P., Jabbar, M.H.A., Gumeci, C., Furuya, Y., Dale, N., Oku, T., Usuda, M., et al. (2023). Lowering the operating temperature of protonic ceramic electrochemical cells to <450 °C. Nat. Energy *8*, 1145–1157. https://doi.org/10.1038/s41560-023-01350-4.
5. Steele, B.C., and Heinzel, A. (2001). Materials for fuel-cell technologies. Nature *414*, 345–352. https://doi.org/10.1038/35104620.
6. Yang, L., Wang, S., Blinn, K., Liu, M., Liu, Z., Cheng, Z., and Liu, M. (2009). Enhanced Sulfur and Coking Tolerance of a Mixed Ion Conductor for SOFCs: BaZr0.1Ce0.7Y0.2-xYbxO3-δ. Science *326*, 126–129. https://doi.org/10.1126/science.1174811.
7. Choi, M., Paik, J., Kim, D., Woo, D., Lee, J., Kim, S.J., Lee, J., and Lee, W. (2021). Exceptionally high performance of protonic ceramic fuel cells with stoichiometric electrolytes. Energy Environ. Sci. *14*, 6476–6483. https://doi.org/10.1039/d1ee01497h.
8. Duan, C., Kee, R.J., Zhu, H., Karakaya, C., Chen, Y., Ricote, S., Jarry, A., Crumlin, E.J., Hook, D., Braun, R., et al. (2018). Highly durable, coking and sulfur tolerant, fuel-flexible protonic ceramic fuel cells. Nature *557*, 217–222. https://doi.org/10.1038/s41586-018-0082-6.
9. Han, L., Zhang, J., Zou, M., and Tong, J.J. (2022). Toward Superb Perovskite Oxide Electrocatalysts: Engineering of Coupled Nanocomposites. Small *18*, e2204784. https://doi.org/10.1002/smll.202204784.
10. Bian, W., Wu, W., Wang, B., Tang, W., Zhou, M., Jin, C., Ding, H., Fan, W., Dong, Y., Li, J., and Ding, D. (2022). Revitalizing interface in protonic ceramic cells by acid etch. Nature *604*, 479–485. https://doi.org/10.1038/s41586-022-04457-y.
11. Zhou, Y., Liu, E., Chen, Y., Liu, Y., Zhang, L., Zhang, W., Luo, Z., Kane, N., Zhao, B., Soule, L., et al. (2021). An Active and Robust Air Electrode for Reversible Protonic Ceramic Electrochemical Cells. ACS Energy Lett. *6*, 1511–1520. https://doi.org/10.1021/acsenergylett.1c00432.
12. Liu, F., Deng, H., Ding, H., Kazempoor, P., Liu, B., and Duan, C. (2023). Process-intensified protonic ceramic fuel cells for power generation, chemical production, and greenhouse gas mitigation. Joule *7*, 1308–1332. https://doi.org/10.1016/j.joule.2023.05.009.
13. Nikodemski, S., Tong, J., and O'Hayre, R. (2013). Solid-state reactive sintering mechanism for proton conducting ceramics. Solid State Ionics *253*, 201–210. https://doi.org/10.1016/j.ssi.2013.09.025.
14. Song, Y., Chen, Y., Wang, W., Zhou, C., Zhong, Y., Yang, G., Zhou, W., Liu, M., and Shao, Z. (2019). Self-Assembled Triple-Conducting Nanocomposite as a Superior Protonic Ceramic Fuel Cell Cathode. Joule *3*, 2842–2853. https://doi.org/10.1016/j.joule.2019.07.004.
15. Tong, J., Clark, D., Hoban, M., and O'Hayre, R. (2010). Cost-effective solid-state reactive sintering method for high conductivity proton conducting yttrium-doped barium zirconium ceramics. Solid State Ionics *181*, 496–503. https://doi.org/10.1016/j.ssi.2010.02.008.
16. Li, G., Jin, H., Cui, Y., Gui, L., He, B., and Zhao, L. (2017). Application of a novel (Pr0.9La0.1)2(Ni0.74Cu0.21Nb0.05)O4+δ-infiltrated BaZr0.1Ce0.7Y0.2O3-δ cathode flor high performance protonic ceramic fuel cells. J. Power Sources *341*, 192–198. https://doi.org/10.1016/j.jpowsour.2016.11.008.
17. Park, S., Vohs, J.M., and Gorte, R.J. (2000). Direct oxidation of hydrocarbons in a solid-oxide fuel cell. Nature *404*, 265–267. https://doi.org/10.1038/35005040.
18. Le, L.Q., Hernandez, C.H., Rodriguez, M.H., Zhu, L., Duan, C., Ding, H., O'Hayre, R.P., and Sullivan, N.P. (2021). Proton-conducting ceramic fuel cells: Scale up and stack integration. J. Power Sources *482*, 228868. https://doi.org/10.1016/j.jpowsour.2020.228868.
19. Zhu, L.Z., O'Hayre, R., and Sullivan, N.P. (2021). High performance tubular protonic ceramic fuel cells via highly-scalable extrusion process. Int. J. Hydrogen Energy *46*, 27784–27792. https://doi.org/10.1016/j.ijhydene.2021.06.018.
20. Tong, G., Li, Y., Wang, Z., and Tan, X. (2023). Batch fabrication of micro-tubular protonic ceramic fuel cells via a phase inversion-based co-spinning/co-sintering technique. J. Power Sources *585*, 233605. https://doi.org/10.1016/j.jpowsour.2023.233605.
21. Costa, R., Hafsaoui, J., Almeida de Oliveira, A.P., Grosjean, A., Caruel, M., Chesnaud, A., and Thorel, A. (2009). Tape casting of proton conducting ceramic material. J. Appl. Electrochem. *39*, 485–495. https://doi.org/10.1007/s10800-008-9671-7.
22. Chen, X., Zhang, H., Li, Y., Xing, J., Zhang, Z., Ding, X., Zhang, B., Zhou, J., and Wang, S. (2021). Fabrication and performance of anode-supported proton conducting solid oxide fuel cells based on BaZr0.1Ce0.7Y0.1Yb0.1O3-δ electrolyte by multi-layer aqueous-based co-tape casting. J. Power Sources *506*, 229922. https://doi.org/10.1016/j.jpowsour.2021.229922.
23. Zhou, T., Huang, H., Meng, Y., Conrad, J., Zou, M., Zhao, Z., Brinkman, K. S., and Tong, J. (2024). Significantly Enhanced Performance of Protonic Ceramic Fuel Cells by Laser Engineering the Electrolyte/Cathode Interface. ACS Energy Lett. *9*, 4557–4563. https://doi.org/10.1021/acsenergylett.4c01785.
24. Chen, T., Jing, Y., Anderson, L.O., Leonard, K., Matsumoto, H., Aluru, N., and Perry, N.H. (2021). Toward Durable Protonic Ceramic Cells: Hydration-Induced Chemical Expansion Correlates with Symmetry in the Y-Doped BaZrO3-BaCeO3 Solid Solution. J. Phys. Chem. C *125*, 26216–26228. https://doi.org/10.1021/acs.jpcc.1c08334.
25. Han, D.L., Liu, X., Bjorheim, T.S., and Uda, T. (2021). Yttrium-Doped Barium Zirconate-Cerate Solid Solution as Proton Conducting Electrolyte: Why Higher Cerium Concentration Leads to Better Performance for Fuel Cells and Electrolysis Cells. Adv. Energy Mater. *11*, 2003149. https://doi.org/10.1002/Aenm.202003149.
26. Loken, A., Ricote, S., and Wachowski, S. (2018). Thermal and Chemical Expansion in Proton Ceramic Electrolytes and Compatible Electrodes. Crystals *8*, 365. https://doi.org/10.3390/Cryst8090365.
27. Gardner, F.J., Day, M.J., Brandon, N.P., Pashley, M.N., and Cassidy, M. (2000). SOFC technology development at Rolls-Royce. J. Power Sources *86*, 122–129. https://doi.org/10.1016/S0378-7753(99)00428-0.
28. Hassmann, K. (2001). SOFC Power Plants, the Siemens-Westinghouse Approach. Fuel Cells *1*, 78–84.
29. Kim, J.H., Song, R.H., Song, K.S., Hyun, S.H., Shin, D.R., and Yokokawa, H. (2003). Fabrication and characteristics of anode-supported flat-tube solid oxide fuel cell. J. Power Sources *122*, 138–143. https://doi.org/10.1016/S0378-7753(03)00431-2.
30. Sui, J., and Liu, J. (2007). An Electrolyte-supported SOFC Stack Fabricated by Slip Casting Technique. ECS Trans. *7*, 633–637. https://doi.org/10.1149/1.2729146.
31. Wetzko, M., Belzner, A., Rohr, F.J., and Harbach, F. (1999). Solid oxide fuel cell stacks using extruded honeycomb type elements. J. Power Sources *83*, 148–155. https://doi.org/10.1016/S0378-7753(99)00289-X.
32. Fergus, J.W. (2005). Sealants for solid oxide fuel cells. J. Power Sources *147*, 46–57. https://doi.org/10.1016/j.jpowsour.2005.05.002.
33. Lai, T.S., and Barnett, S.A. (2005). Design considerations for segmented-in-series fuel cells. J. Power Sources *147*, 85–94. https://doi.org/10.1016/j.jpowsour.2005.01.002.
34. An, Y.T., Ji, M.J., Hwang, H.J., Eugene Park, S., and Choi, B.H. (2015). Effect of cell-to-cell distance in segmented-in-series solid oxide fuel cells. Int. J. Hydrogen Energy *40*, 2320–2325. https://doi.org/10.1016/j.ijhydene.2014.11.133.
35. An, Y.T., Ji, M.J., Hwang, H.J., Park, S.E., and Choi, B.H. (2015). Effect of cell length on the performance of segmented-in-series solid oxide fuel cells fabricated using decalcomania method. J. Ceram. Soc. Jpn. *123*, 178–181. https://doi.org/10.2109/jcersj2.123.178.
36. Fujita, K., Seyama, T., Sobue, T., and Matsuzaki, Y. (2012). Development of segmented-in-series-type solid oxide fuel cells for residential applications. Energy Proc. *28*, 153–161. https://doi.org/10.1016/j.egypro.2012.08.049.

37. Fujita, K., Somekawa, T., Horiuchi, K., and Matsuzaki, Y. (2009). Evaluation of the redox stability of segmented-in-series solid oxide fuel cell stacks. J. Power Sources *193*, 130–135. https://doi.org/10.1016/j.jpowsour.2008.11.091.
38. Liu, B., Muroyama, H., Matsui, T., Tomida, K., Kabata, T., and Eguchi, K. (2010). Analysis of Impedance Spectra for Segmented-in-Series Tubular Solid Oxide Fuel Cells. J. Electrochem. Soc. *157*, B1858–B1864. https://doi.org/10.1149/1.3494214.
39. Lai, T.S., Liu, J., and Barnett, S.A. (2004). Effect of cell width on segmented-in-series SOFCs. Electrochem. Solid State Lett. *7*, A78–A81. https://doi.org/10.1149/1.1649398.
40. Park, B.K., Kim, D.W., Song, R.H., Lee, S.B., Lim, T.H., Park, S.J., Park, C.O., and Lee, J.W. (2015). Design of a dual-layer ceramic interconnect based on perovskite oxides for segmented-in-series solid oxide fuel cells. J. Power Sources *300*, 318–324. https://doi.org/10.1016/j.jpowsour.2015.09.082.
41. Pillai, M.R., Gostovic, D., Kim, I., and Barnett, S.A. (2007). Short-period segmented-in-series solid oxide fuel cells on flattened tube supports. J. Power Sources *163*, 960–965. https://doi.org/10.1016/j.jpowsour.2006.09.079.
42. Xiao, H., Tong, J., Peng, F., Brinkman, K.S., Mu, S., Jincheng, L.E.I., Hong, Y., Huang, H., and Bordia, R. (2020). Integrated additive manufacturing and laser processing systems and methods for ceramic, glass, and silicon carbide applications. patent application US17/138,173.
43. Han, G.D., Bae, K., Kang, E.H., Choi, H.J., and Shim, J.H. (2020). Inkjet Printing for Manufacturing Solid Oxide Fuel Cells. ACS Energy Lett. *5*, 1586–1592. https://doi.org/10.1021/acsenergylett.0c00721.
44. Sukeshini A, M., Meisenkothen, F., Gardner, P., and Reitz, T.L. (2013). Aerosol Jet® Printing of functionally graded SOFC anode interlayer and microstructural investigation by low voltage scanning electron microscopy. J. Power Sources *224*, 295–303. https://doi.org/10.1016/j.jpowsour.2012.09.094.
45. Tai, X.Y., Zhakeyev, A., Wang, H., Jiao, K., Zhang, H., and Xuan, J. (2019). Accelerating Fuel Cell Development with Additive Manufacturing Technologies: State of the Art, Opportunities and Challenges. Fuel Cells *19*, 636–650. https://doi.org/10.1002/fuce.201900164.
46. Zhu, Z., Gong, Z., Qu, P., Li, Z., Rasaki, S.A., Liu, Z., Wang, P., Liu, C., Lao, C., and Chen, Z. (2021). Additive manufacturing of thin electrolyte layers via inkjet printing of highly-stable ceramic inks. J. Adv. Ceram. *10*, 279–290. https://doi.org/10.1007/s40145-020-0439-9.
47. Zouridi, L., Garagounis, I., Vourros, A., Marnellos, G.E., and Binas, V. (2022). Advances in Inkjet-Printed Solid Oxide Fuel Cells. Adv. Mater. Technol. *7*, 2101491. https://doi.org/10.1002/Admt.202101491.
48. Manogharan, G., Kioko, M., and Linkous, C. (2015). Binder Jetting: A Novel Solid Oxide Fuel-Cell Fabrication Process and Evaluation. Jom *67*, 660–667. https://doi.org/10.1007/s11837-015-1296-9.
49. Kim, S., Lee, H., Kim, C., Jang, I., Lee, K., Sun, S., Lee, D., Kim, J., Park, K., Lee, G., et al. (2022). Interface-reinforcing sintering step for highly stable operation of proton-conducting fuel cell stack. J. Power Sources *548*, 232082. https://doi.org/10.1016/j.jpowsour.2022.232082.
50. Ishii, A., Mu, S., Meng, Y., Huang, H., Lei, J., Li, Y., Peng, F., Xiao, H., Tong, J., and Brinkman, K.S. (2020). Rapid Laser Processing of Thin Sr-Doped LaCrO3-δ Interconnects for Solid Oxide Fuel Cells. Energy Technol. *8*, 2000364. https://doi.org/10.1002/Ente.202000364.
51. Mu, S.L. (2020). Manufacturing of Protonic Ceramic Energy Devices by a Novel Integrated Additive Manufacturing and Laser Processing.
52. Mu, S., Hong, Y., Huang, H., Ishii, A., Lei, J., Song, Y., Li, Y., Brinkman, K.S., Peng, F., Xiao, H., and Tong, J. (2020). A Novel Laser 3D Printing Method for the Advanced Manufacturing of Protonic Ceramics. Membranes *10*, 98. https://doi.org/10.3390/membranes10050098.
53. Mu, S., Huang, H., Ishii, A., Hong, Y., Santomauro, A., Zhao, Z., Zou, M., Peng, F., Brinkman, K.S., Xiao, H., and Tong, J. (2020). Rapid Laser Reactive Sintering for Sustainable and Clean Preparation of Protonic Ceramics. ACS Omega *5*, 11637–11642. https://doi.org/10.1021/acsomega.0c00879.
54. Mu, S., Huang, H., Ishii, A., Zhao, Z., Zou, M., Kuzbary, P., Peng, F., Brinkman, K.S., Xiao, H., and Tong, J. (2020). Rapid laser reactive sintering of BaCe(0)(.7)Zr(0.1)Y(0.1)Yh(0.1)O(3-δ) electrolyte for protonic ceramic fuel cells. J. Power Source Adv. *4*, 100017. https://doi.org/10.1016/J.Powera.2020.100017.
55. Mu, S., Zhao, Z., Lei, J., Hong, Y., Hong, T., Jiang, D., Song, Y., Jackson, W., Brinkman, K.S., Peng, F., et al. (2018). Engineering of microstructures of protonic ceramics by a novel rapid laser reactive sintering for ceramic energy conversion devices. Solid State Ionics *320*, 369–377. https://doi.org/10.1016/j.ssi.2018.03.023.
56. Zou, M., Conrad, J., Sheridan, B., Zhang, J., Huang, H., Mu, S., Zhou, T., Zhao, Z., Brinkman, K.S., Xiao, H., et al. (2023). 3D Printing Enabled Highly Scalable Tubular Protonic Ceramic Fuel Cells. ACS Energy Lett. *8*, 3545–3551. https://doi.org/10.1021/acsenergylett.3c01345.
57. Tong, J., Clark, D., Bernau, L., Sanders, M., and O'Hayre, R. (2010). Solid-state reactive sintering mechanism for large-grained yttrium-doped barium zirconate proton conducting ceramics. J. Mater. Chem. *20*, 6333–6341. https://doi.org/10.1039/c0jm00381f.
58. Liu, S., and Shin, Y.C. (2020). Prediction of 3D microstructure and phase distributions of Ti6Al4V built by the directed energy deposition process via combined multi-physics models. Addit. Manuf. *34*, 101234. https://doi.org/10.1016/J.Addma.2020.101234.
59. Zheng, M., Wang, G., Zhou, W., Wei, L., Lin, X., and Huang, W. (2023). Understanding grain evolution in laser powder bed fusion process through a real-time coupled Lattice Boltzmann model-Cellular Automaton simulation. J. Mater. Process. Technol. *321*, 118126. https://doi.org/10.1016/j.jmatprotec.2023.118126.
60. Choi, S.M., Lee, J.H., Hong, J., Kim, H., Yoon, K.J., Kim, B.K., and Lee, J.H. (2014). Effect of sintering atmosphere on phase stability, and electrical conductivity of proton-conducting Ba(Zr0.84Y0.15Cu0.01)O3-δ. Int. J. Hydrogen Energy *39*, 7100–7108. https://doi.org/10.1016/j.ijhydene.2014.02.072.
61. Loureiro, F.J.A., Nasani, N., Reddy, G.S., Munirathnam, N.R., and Fagg, D.P. (2019). A review on sintering technology of proton conducting BaCeO3-BaZrO3 perovskite oxide materials for Protonic Ceramic Fuel Cells. J. Power Sources *438*, 226991. https://doi.org/10.1016/j.jpowsour.2019.226991.
62. Yamazaki, Y., Hernandez-Sanchez, R., and Haile, S.M. (2010). Cation nonstoichiometry in yttrium-doped barium zirconate: phase behavior, microstructure, and proton conductivity. J. Mater. Chem. *20*, 8158–8166. https://doi.org/10.1039/c0jm02013c.
63. Kim, D., Bae, K.T., Kim, K.J., Im, H.N., Jang, S., Oh, S., Lee, S.W., Shin, T.H., and Lee, K.T. (2022). High-Performance Protonic Ceramic Electrochemical Cells. ACS Energy Lett. *7*, 2393–2400. https://doi.org/10.1021/acsenergylett.2c01370.
64. Wang, C., Ping, W., Bai, Q., Cui, H., Hensleigh, R., Wang, R., Brozena, A.H., Xu, Z., Dai, J., Pei, Y., et al. (2020). A general method to synthesize and sinter bulk ceramics in seconds. Science *368*, 521–526. https://doi.org/10.1126/science.aaz7681.
65. Duan, C., Kee, R., Zhu, H., Sullivan, N., Zhu, L., Bian, L., Jennings, D., and O'Hayre, R. (2019). Highly efficient reversible protonic ceramic electrochemical cells for power generation and fuel production. Nat. Energy *4*, 230–240. https://doi.org/10.1038/s41560-019-0333-2.
66. Geng, C., Yu, X., Wang, P., Cheng, J., and Hong, T. (2020). The rapid one-step fabrication of bilayer anode for protonic ceramic fuel cells by phase inversion tape casting. J. Eur. Ceram. Soc. *40*, 3104–3110. https://doi.org/10.1016/j.jeurceramsoc.2020.02.020.
67. He, F., Liang, M., Wang, W., Ran, R., Yang, G., Zhou, W., and Shao, Z. (2020). High-Performance Proton-Conducting Fuel Cell with B-Site-Deficient Perovskites for All Cell Components. Energ Fuel *34*, 11464–11471. https://doi.org/10.1021/acs.energyfuels.0c02370.

Please cite this article in press as: Huang et al., Scalable, durable, and high-performance protonic ceramic fuel cell stacks manufactured by direct laser reactive additive manufacturing, Device (2025), https://doi.org/10.1016/j.device.2025.100840

68. Kim, C., Lee, H., Jang, I., Kim, S., Jung, H., Ryu, M., Kim, J., Lee, D., Yoon, H., Paik, U., and Song, T. (2022). BaCo0.4Fe0.4Zr0.1Y0.1O3-δ triple conductor for boosting electrode efficiency for proton conducting fuel cells. Int. J. Hydrogen Energy *47*, 5499–5506. https://doi.org/10.1016/j.ijhydene.2021.11.140.

69. Liang, M., He, F., Zhou, C., Chen, Y., Ran, R., Yang, G., Zhou, W., and Shao, Z. (2021). Nickel-doped BaCo0.4Fe0.4Zr0.1Y0.1O3-δ as a new high-performance cathode for both oxygen-ion and proton conducting fuel cells. Chem. Eng. J. *420*, 127717. https://doi.org/10.1016/J.Cej.2020.127717.

70. Ma, J., Zhu, F., Pan, Y., Zhang, H., Xu, K., Wang, Y., and Chen, Y. (2022). A Y-doped BaCo0.4Fe0.4Zn0.2O3-δ perovskite air electrode with enhanced CO2 tolerance and ORR activity for protonic ceramic electrochemical cells. Sep. Purif. Technol. *288*, 120657. https://doi.org/10.1016/J.Seppur.2022.120657.